Plasmoid formation and strong radiative cooling in a driven magnetic reconnection experiment

R. Datta,[1] K. Chandler,[2] C.E. Myers,[2,*] J. P. Chittenden,[3] A. J. Crilly,[3] C. Aragon,[2] D. J. Ampleford,[2] J. T. Banasek,[2] A. Edens,[2] W. R. Fox,[4] S. B. Hansen,[2] E. C. Harding,[2] C. A. Jennings,[2] H. Ji,[4] C. C. Kuranz,[5] S. V. Lebedev,[3] Q. Looker,[2] S. G. Patel,[2] A. Porwitzky,[2] G. A. Shipley,[2] D. A. Uzdensky,[6] D. A. Yager-Elorriaga,[2] and J.D. Hare[1,†]

[1]*Plasma Science and Fusion Center, Massachusetts Institute of Technology, MA 02139, Cambridge, USA*
[2]*Sandia National Laboratories, Albuquerque, NM 87123-1106, USA*
[3]*Blackett Laboratory, Imperial College London, London SW7 2BW, UK*
[4]*Princeton Plasma Physics Laboratory, Princeton, NJ 08543, USA*
[5]*Department of Nuclear Engineering and Radiological Sciences, University of Michigan, Ann Arbor, MI 48109, USA*
[6]*Center for Integrated Plasma Studies, Physics Department, UCB-390, University of Colorado, Boulder, Colorado, USA*

We present the first experimental study of plasmoid formation in a magnetic reconnection layer undergoing rapid radiative cooling, a regime relevant to extreme astrophysical plasmas. Two exploding aluminum wire arrays, driven by the Z machine, generate a reconnection layer ($S_L \approx 120$) in which the cooling rate far exceeds the hydrodynamic transit rate ($\tau_{\rm hydro}/\tau_{\rm cool} > 100$). The reconnection layer generates a transient burst of >1 keV X-ray emission, consistent with the formation and subsequent rapid cooling of the layer. Time-gated X-ray images show fast-moving (up to $50\,{\rm km\,s^{-1}}$) hotspots in the layer, consistent with the presence of plasmoids in 3D resistive magnetohydrodynamic simulations. X-ray spectroscopy shows that these hotspots generate the majority of Al K-shell emission (around 1.6 keV) prior to the onset of cooling, and exhibit temperatures (170 eV) much greater than that of the plasma inflows and the rest of the reconnection layer, thus providing insight into the generation of high-energy radiation in radiatively-cooled reconnection events.

Magnetic reconnection is a ubiquitous process in magnetized plasmas, that explosively converts magnetic energy into heat and kinetic energy [1–3]. In extreme astrophysical systems, such as black hole accretion disks [4–7], pulsar magnetospheres [8–11], and gamma-ray bursts [12–16], strong radiative cooling (e.g. inverse external Compton or synchrotron cooling) can remove internal energy faster than it is injected into the reconnection layer [15, 17, 18]. Theory predicts that this can trigger a radiative collapse — a runaway cooling and compression process — that generates a dense, cold layer with a faster reconnection rate [17, 19].

Despite the importance of radiative cooling, there has been limited laboratory investigation of radiatively-cooled reconnection, as it is difficult to achieve cooling rates necessary for significant cooling on experimental time scales. Previous magnetically-driven experiments, such as MRX ($n_e \sim 10^{13}\,{\rm cm^{-3}}, T_e \sim 10\,{\rm eV}, \beta \ll 1$) [2, 20], have investigated a variety of reconnection physics [20–23] in a low-density regime with negligible radiative cooling. In contrast, laser-driven experiments [24–28] access a strongly-driven $\beta \gg 1$ high-energy-density (HED) regime ($n_e \sim 10^{20}\,{\rm cm^{-3}}, T_e \sim 1000\,{\rm eV}$) [24]. However, the fully-stripped ions in the reconnection layer at these high temperatures [27, 29] prevent line emission, and the cooling parameter $R_{\rm cool} \equiv \tau_{\rm hydro}/\tau_{\rm cool}$ remains small. Pulsed-power driven reconnection experiments access a complementary, strongly-driven $\beta \approx 1$ HED regime [30]. Experiments on the 1.4 MA MAGPIE facility ($n_e \sim 10^{18}\,{\rm cm^{-3}}, T_e \sim 50\,{\rm eV}$)[30–32] either observed plasmoid formation with minimal cooling at higher Lundquist numbers $S_L \sim 100$ [33], or sudden ion cooling at a lower $S_L < 10$ [34].

This Letter presents results from the Magnetic Reconnection on Z (MARZ) experiments, which generate a radiatively-cooled reconnection layer by driving a dual exploding wire array using the Z machine (20 MA, 300 ns rise time, Sandia National Labs) [35]. Unlike previous pulsed-power experiments, the MARZ experiments demonstrate both a high $S_L \sim 100$ and a high cooling parameter ($R_{\rm cool} > 100$). We make the first quantitative measurements of reconnection in a strongly radiatively-cooled regime, using temporally- and spatially-resolved X-ray diagnostics to measure emission from the reconnection layer. This is of particular astrophysical significance, as radiative emission is the key, and often only, signature of reconnection in extreme astrophysical objects [15]. We observe the formation and subsequent radiative cooling of the reconnection layer. Furthermore, the layer exhibits sub-millimeter-scale fast-moving hotspots that emit most of the high-energy X-rays from the layer. Radiative resistive magnetohydrodynamic (MHD) simulations of the experiment [36] show that these hotspots are likely to be plasmoids generated by the tearing instability [37]. These simulations, performed in GORGON [38], implement $P_{1/3}$ multi-group radiation transport, using emissivities and opacities from SpK [39]. We use these simulations, which are detailed in Ref. [36], to guide the interpretation of the experimental results in this Letter.

Figure 1a shows the experimental setup, comprising two 40 mm tall, 40 mm diameter exploding wire arrays, each with 150 equally-spaced 75 µm diameter aluminum wires. The arrays have a 60 mm center-to-center separation, with a 10 mm gap between the mid-plane and the wires. Each array generates radially diverging plasma flows with azimuthally-oriented frozen-in magnetic field that is advected with the flow [31–34, 40]. The outflows collide at the mid-plane, where the anti-parallel magnetic fields generate a reconnection layer. The arrays are driven in parallel by the Z machine; Figure 1b shows the current $I(t)$ measured by a b-dot probe near the load [41], which is well approximated by $I(t) = 20\,{\rm MA}\sin^2(\pi/2 \times t/300\,{\rm ns})$. Photonic Doppler ve-

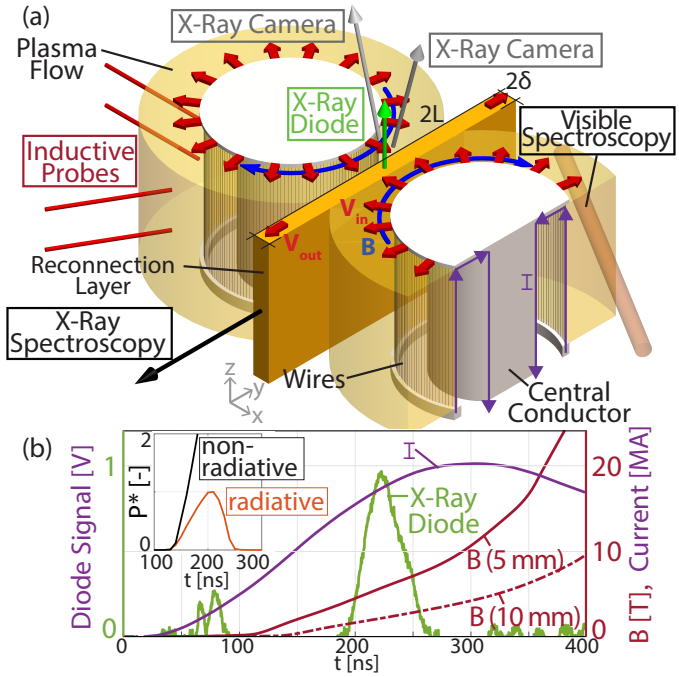

FIG. 1: (a) A three-dimensional model of the dual wire array load and diagnostic setup. (b) Current (purple), X-ray diode signal (green), and magnetic field at 5 mm and 10 mm from the wires (red). Inset: Simulated X-Ray emission from the reconnection layer, filtered with 8 µm Be, for non-radiative (black) and radiatively-cooled (orange) cases. X-ray power P^* is normalized using the peak power in the radiatively-cooled simulation.

locimetry [42] measured equal current division between the arrays across multiple shots. The arrays are over-massed, so they generate continuous plasma flows from stationary wire cores throughout the experiment without exploding [43, 44]. The discrete plasma flows from adjacent wire cores are expected to form a dense network of oblique shocks due to their azimuthal expansion [31, 34, 45]. The plasma flows are highly-collisional ($\lambda_{ii} \approx 1-10$ nm), strongly-driven ($M_A \approx 7$, $M_S > 10$), and quasi-2D with minimal variation along z. There is no guide field, and the ion skin depth ($d_i \approx 0.1$ mm) is small compared to the reconnection layer width (~ 1 mm).

We use inductive probes and visible spectroscopy to characterize the magnetic field, ion density, and electron temperature in the outflows from the arrays, which form the inflows into the reconnection layer. Calibrated inductive probes [46] are positioned at different radii (5 mm & 10 mm) around the arrays (Figure 1a). Opposite-polarity probe pairs with a 1 cm vertical separation are used at each location for redundancy and to check for the common mode [47, 48]. The magnetic field is determined by numerically integrating the signals. The magnetic fields $B(t)$ measured at 5 mm and 10 mm are similar in shape, but displaced in time (Figure 1b), consistent with the advection of the field between the probes at a velocity of $140 \pm 30\,\mathrm{km\,s^{-1}}$ [47].

We use an optical fiber to collect visible radiation from the plasma along a path (diameter ≈ 4 mm) in the xy plane, centered 8 mm from the wires, to a spectrometer ($400-700$ nm range, 1.5 nm resolution) coupled to a streak camera (550 ns sweep time) [49]. The spectra show Al-II and Al-III emission lines. We infer density from the width of the well-isolated Al-II 466.4 nm line, and temperature from the line ratio of the inter-stage Al-II 466.4 nm and Al-III 448.1 nm, 452.4 nm lines. This is done by fitting synthetic spectra, generated using PrismSPECT and radiation transport simulations, to the experimental data [50, 51]. The electron temperature in the array outflows increases from (1.8 ± 0.4) eV to (2.1 ± 0.4) eV between $200-240$ ns, and the ion density is $5-8 \times 10^{17}\,\mathrm{cm^{-3}}$.

A filtered X-ray diode viewing the reconnection layer from the top (vertical green arrow in Figure 1a) provides time-resolved measurements of the emitted X-ray power. The 8 µm beryllium filter transmits photons with energy >1 keV. X-ray emission from the reconnection layer (Figure 1b) exhibits a sharp peak at 220 ns, with a full-width-at-half-maximum of about 50 ns. The signal is reproducible over multiple shots and viewing angles. The X-ray emission is narrower than the driving current pulse, and reaches a maximum before peak current, indicating that this signal is driven by dynamics of the reconnection layer, rather than the driving current.

We probe the temporal evolution of the reconnection layer with two ultra-fast X-ray imaging pinhole cameras [52]. The cameras (4 frames, 10 ns exposure) provide a $25 \times 12.5\,\mathrm{mm^2}$ field of view through a 500 µm diameter pinhole (magnification = 1×, geometric resolution ≈ 1 mm), filtered with 2 µm-thick aluminized mylar (>100 eV photons). The cameras view the reconnection layer with polar angles of $\theta = 9°$ and $\theta = 12°$ respectively, and with azimuthal angles (from the $x-$axis) of $\phi = 170°$ and $\phi = 40°$, thus viewing both the top and side of the layer (see Figure 1a). Figure 2 (a-c) show an elongated, bright layer with strongly-emitting, localized (~ 1 mm size) hotspots (indicated by green arrows) between $200-240$ ns. The intensity of the emission initially increases, peaking at 220 ns, and then decreases. Figure 2 shows images from only one camera ($\theta = 12°$, $\phi = 40°$); images from the second camera, containing similar features, are in the supplementary material. The hotspots move along the y-direction, away from the center of the layer. From the translation of the hotspots between $220-240$ ns, we estimate their velocity (Figure 2e), which shows acceleration from rest to $50 \pm 20\,\mathrm{km\,s^{-1}}$ over 10 mm. We show later that this is consistent with the expected and simulated outflow velocity from the layer.

An X-ray spectrometer with a spherically-bent crystal [53] provides time-integrated spatially-resolved (along z, resolution: $\Delta z \approx 200$ µm) spectral measurements (resolution: $\Delta E \approx 0.5$ eV) of X-ray emission from the reconnection layer (see Figure 1a). Figure 3a shows the X-ray spectrum, which exhibits He-like and Li-like satellite Al K-shell transitions with energies of about 1.6 keV. These transitions are labeled in Figure 3b, which shows a lineout of the recorded spectrum averaged over $z = 10 \pm 1$ mm. We show the X-ray spectrum from the same experimental shot as the diode signal and X-ray images; however, this spectrum is reproducible across multiple shots. Although the spectrum is time-integrated, the fil-

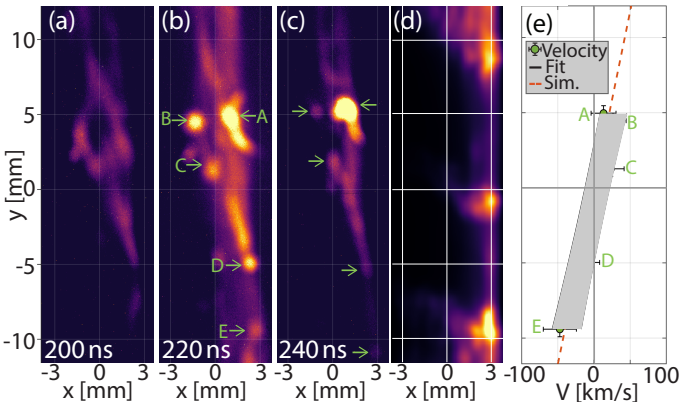

FIG. 2: (a-c) Time-gated X-ray images (10 ns exposure) of the reconnection layer, showing hotspots (green arrows) inside a bright elongated layer. (d) Synthetic X-ray image of the layer obtained by post-processing a 3D simulation at 220 ns with X-ray emission and radiation transport modeling [36]. (e) Velocity of the hotspots inside the reconnection layer. The solid line is a linear fit to the hotspot velocity, and dashed orange line is the simulated outflow velocity in the reconnection layer, averaged between $200-250$ ns.

tered X-ray diode (8 μm Be, >1 keV) temporally localizes the spectra to 220 ± 25 ns.

Combining the spatial, temporal, and spectral measurements of the X-ray emission provides information about the evolution of the reconnection layer. The narrow burst of X-ray emission from the layer, as recorded simultaneously by the diode (Figure 1b) and X-ray cameras (Figure 2), provides evidence for formation and radiative cooling of the layer. The initial rise of the diode signal indicates increasing density and/or temperature of the layer during formation. The layer temperature is initially hot enough to generate >1 keV emission. The sharp fall in the X-ray emission after 220 ns is consistent

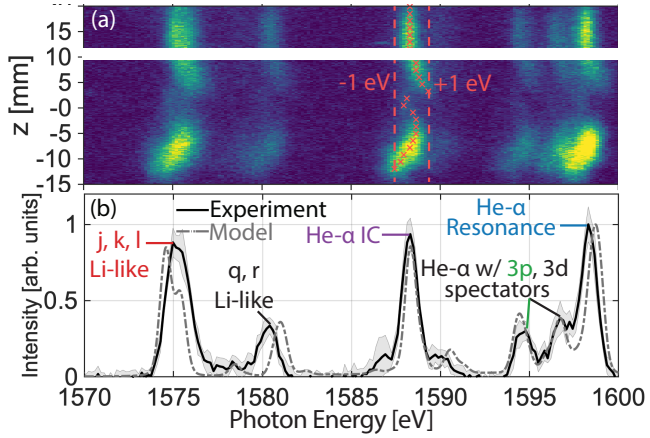

FIG. 3: (a) Time-integrated X-ray spectra from the reconnection layer showing Al K-shell emission. Red crosses show the position of the He-α inter-combination line. (b) X-ray spectrum averaged over $z=(10\pm1)$ mm [white line in (a)] showing He-like and Li-like satellite transitions (black), and calculated spectrum from the SCRAM and radiation transport model for 170 eV, 1×10^{18} cm^{-3} hotspot density, and 0.5 mm hotspot size (grey dashed).

with a rapidly cooling reconnection layer. X-ray images of the layer exhibit a similar intensity evolution as the diode, with a maximum intensity around 220 ns (Figure 2). Resistive MHD simulations confirm that X-ray emission from the reconnection layer provides a diagnostic signature of strong radiative cooling [36]: in the absence of radiative cooling, simulations show that X-ray emission (>1 keV) would continue to rise due to increasing layer density at a constant, high temperature, as shown by the black curve in the inset of Figure 1b. However, radiative cooling results in a sharp decline in the simulated X-ray emission after an initial rise (orange curve, Figure 1b), similar to the experimentally-measured emission.

To obtain quantitative measurements of temperature and density in the reconnection layer from the X-ray spectra in Figure 3 during the onset of radiative cooling, we use non-local thermodynamic equilibrium spectral emissivities and absorption opacities generated using SCRAM [54] to model radiation transport [55] along the diagnostic line-of-sight. SCRAM includes spectral line broadening effects, and incorporates photo-pumping by assuming cylindrical geometry with diameter of 1 mm. These radiation transport calculations constrain the composition of the emitting plasma: because of the higher opacity of the He-α resonance transition compared to the other lines in Figure 3b, it is strongly damped in homogeneous layers of length >1 mm. Therefore, only sub-millimeter-sized hotspots, strongly emitting in the Al K-shell, can account for the similar measured intensities of the He-α resonance and inter-combination (IC) lines. The experimental spectrum is best matched by the emission from localized, dense hotspots of size <1 mm and $T_e\approx(170\pm30)$ eV, embedded within a colder, less dense reconnection layer. An example spectrum calculated assuming emission from a single hotspot of size $d=0.5$ mm, temperature $T_e=170$ eV, and ion density $n_i=1\times10^{18}$ cm^{-3} in a non-emitting non-absorbing layer, is shown by the dashed curve in Figure 3b, and reproduces the line ratios and line widths of the experimental spectrum. The model includes the effect of source and instrument broadening, but neglects Doppler shift, which is <0.25 eV, as calculated from the hotspot velocities (in Figure 2e). Radiation transport also provides an upper limit of about 75 eV on the layer temperature, to prevent over-damping of the He-α resonance line generated from the hotspots. This model is further supported by X-ray images of the layer (Figure 2), which show brightly-emitting hotspots <1 mm in size inside the less brightly-emitting reconnection layer. Figure 3a further shows that the hotspots form contiguous structures, elongated along z by ~10 mm.

To constrain the density (n_i), temperature (T_e), and size (d) of the hotspots for which the experimental X-ray spectrum is valid, we uniformly and randomly sample values of n_i, T_e, and d to obtain solutions that match within 20% the experimentally observed line ratios. Comparing the relative intensities of the He-α IC with the Li-j satellite line and He-α with 3p spectator transition constrains T_e to a narrow band around (170 ± 30) eV, and provides an upper bound of $\sim5\times10^{18}$ cm^{-3} on the hotspot ion density. Assuming

TABLE I: Plasma parameters in the pre-shock inflow, post-shock inflow, and reconnection layer at 220 ns. Values in bold are measured experimentally, while other values are estimated/inferred.

	n_i [cm^{-3}]	T_e [eV]	$\bar{Z}$	B_y [T]	$V_x(V_y)$ [km/s]	V_A [km/s]	C_S [km/s]
Pre-shock	$\mathbf{0.8\times10^{18}}$	**1.9**	**1.9**	**3.9**	**140** (-)	20	5
Post-shock	6×10^{18}	30	8.0	30	20 (-)	50	30
Layer	6×10^{18}	60	10.3	-	- (**72**)	-	50

that the hotspot density lies between the upper bound of $n_i \leq 5\times10^{18}\,\mathrm{cm}^{-3}$ and the lower bound of $n_i \geq 5\times10^{17}\,\mathrm{cm}^{-3}$ (inflow density from visible spectroscopy), this sampling constrains $0.3 \leq d \leq 0.5\,\mathrm{mm}$.

We also observe hotspots in synthetic X-ray images produced from 3D resistive MHD simulations of the experiment [36] (Figure 2d). In these simulations, plasmoids which grow from random perturbations in the current sheet via the tearing instability, are hotter and denser than the rest of the layer, and therefore generate intense Al K-shell X-ray emission [36]. Figure 2(a-d) show qualitative agreement in the layer structure between the experiment and simulation, showing hotspots of diameter $< 1\,\mathrm{mm}$ embedded in a thin, less brightly emitting layer. The experimentally measured hotspot velocity is also consistent with the simulated velocity in the outflows from the reconnection layer, as seen in Figure 2e. The plasmoid instability in the simulations occurs at Lundquist numbers below the canonical critical value $S_L^* \sim 10^4$, suggesting a departure from the original tearing theory [37, 56]. This discrepancy may arise from compressibility, non-uniform plasma resistivity, or density perturbations introduced by the discrete wires [36]. The simulations further show that the presence of plasmoids does not increase the reconnection rate above the radiatively-cooled Sweet-Parker prediction [17].

These 3D simulations show that the plasmoid position in the xz-plane varies along z, due to the MHD kink instability [36]. We see preliminary evidence for this modulation in the axially-resolved X-ray spectrum (Figure 3a), where the spectral positions of the lines exhibit modulations of up to 1 eV along z. Ray tracing calculations [53] show that these deviations correspond to 1 mm x-displacements in the source position, comparable to the simulated kink instability amplitude.

Using these experimental measurements, we calculate key parameters for the inflows and the reconnection layer using simple analytical models. Table I summarizes the experimentally determined parameters in the layer inflows (array outflows) right before onset of radiative cooling (220 ns). The magnetic field is averaged from probe measurements at 5 and 10 mm, while n_i and T_e are from visible spectroscopy. From these, we estimate the thermal pressure p, adiabatic index $\gamma \approx 1.2$ [55], and the Alfvén $V_A = B/\sqrt{\mu_0\rho}$ and sound speeds $C_S = \sqrt{\gamma p/\rho}$. We assume $T_i \approx T_e$ as the estimated energy equilibration time $\tau_E \approx 2\,\mathrm{ns}$ [57] is smaller than the hydrodynamic time $\tau_{\mathrm{hydro}} = L/V \approx 70\,\mathrm{ns}$. Values of effective ionization $\bar{Z}$ in Table I are calculated for the given n_i and T_e using a Thomas-Fermi model [38, 58], the results of which agree well with PrismSPECT and SCRAM calculations.

The layer inflows are super-Alfvénic ($M_A \approx 7$); consequently we expect magnetic flux pile-up to generate shocks upstream of the layer, dividing the inflow into pre-shock and post-shock regions, as observed in the simulations [36] and previous experiments [31, 34, 59, 60]. We estimate the post-shock conditions from analytical solutions of the Rankine-Hugoniot equations for a fast, perpendicular MHD shock [61, 62], which increases the density and magnetic field, and decreases the inflow velocity, by a factor of about 8. Estimated values in the post-shock inflow are shown in Table I.

To estimate the parameters in the reconnection layer, we assume: (1) a pressure balance exists between the layer and the post-shock inflow; (2) right before onset of cooling, there is little compression of the layer, such that n_i is roughly equal inside and just outside the layer in the post-shock inflow. Both assumptions are expected from theory [17], and supported by simulations [36]. The estimated layer temperature and ion density at this time are therefore 60 eV and $6\times10^{18}\,\mathrm{cm}^{-3}$. The temperature is below the upper bound ($T_e \lesssim 75\,\mathrm{eV}$), while the density is close to the upper bound ($n_i \lesssim 5\times10^{18}\,\mathrm{cm}^{-3}$) determined from X-ray spectroscopy.

We extrapolate the linear velocity trend in Figure 2e to $y = L$ ($L = 15\,\mathrm{mm}$, $0.5\times$ field line radius of curvature at the mid-plane), and estimate the layer outflow velocity $V_{out} \approx 72\,\mathrm{km\,s}^{-1}$. We have assumed that the plasmoids have a velocity similar to bulk layer velocity, since they are advected along $\pm y$ by the plasma outflows [37, 56, 63]. The estimated outflow velocity closely matches the magnetosonic velocity $V_{MS} = (V_{A,in}^2 + C_{S,L}^2)^{0.5} \approx 70\,\mathrm{km\,s}^{-1}$ (computed from the Alfvén speed outside the layer $V_{A,in}$, and the sound speed inside the layer $C_{S,L}$), which is the theoretical outflow velocity from the reconnection layer [21, 33]. The estimated Lundquist number is $S_L = LV_A/\bar{\eta} \approx 120$, and the predicted Sweet-Parker layer width is $\delta_{SP} \approx L(S_L)^{-1/2} \approx 1.4\,\mathrm{mm}$ [1, 2]. This width is much larger than both the estimated ion-ion mean free path ($\lambda_{ii} \approx 2\,\mathrm{nm}$) and the ion skin depth ($d_i \approx 0.1\,\mathrm{mm}$), indicating high collisionality, and justifying the use of resistive MHD models. Using the post-shock inflow velocity $V_{in} \approx 20\,\mathrm{km\,s}^{-1}$, we infer the reconnection rate at this time $V_{in}/V_{out} \approx 0.3$, which is roughly comparable to the Sweet-Parker rate $S_L^{-1/2} \approx 0.1$ [1].

Finally, we make order-of-magnitude estimates of the dominant terms in the layer power balance. The estimated Ohmic and compressional heating are $P_\Omega \sim \eta j^2 \sim \eta[B_{in}/(\delta_{SP}\mu_0)]^2 \sim 10^{15}\,\mathrm{W\,m}^{-3}$ and $P_{\mathrm{comp}} \sim pV_{in}/\delta_{SP} \sim 10^{16}\,\mathrm{W\,m}^{-3}$. Viscous heating and thermal conduction are negligible. We estimate the radiative loss from the layer by solving the radiation transport equation along a mean chord with a length approximated as the volume-to-surface area ratio of a rectangular slab of width 2δ and length $2L$ [36]. Using emissivities and opacities from SpK [39], the resulting loss rate is $P_{\mathrm{rad}} \sim 10^{18}\,\mathrm{W\,m}^{-3}$, corresponding to a cooling parameter $R_{\mathrm{cool}} \sim 400$ at 220 ns. The experimentally-measured hotspot temperature and density provide an upper bound on the cooling rate $P_{\mathrm{rad,\,hotspot}} \sim$

$10^{19}\,\mathrm{W\,m^{-3}}$. Cooling therefore dominates heating within the reconnection layer, consistent with the strong cooling observed in Figure 1(b) & Figure 2(a-c).

In summary, we present the first experimental evidence of strong radiative cooling in a pulsed-power-driven reconnection experiment with $S_L > 100$. The key results are:
1. The reconnection layer exhibits millimeter-scale fast-moving hotspots with strong X-ray emission, consistent with the presence of magnetic islands generated by the plasmoid instability in 3D resistive MHD simulations (Figure 2).
2. The majority of the high-energy X-rays are generated by these hotspots, which exhibit a temperature (about 170 eV) higher than both the inflow (about 2 eV) and bulk layer temperature (<75 eV) (Figure 3).
3. The reconnection layer undergoes strong radiative cooling, characterized by the rapid decrease in X-ray emission from the layer (Figure 1b, Figure 2).

Strong cooling is necessary to trigger radiative collapse of the reconnection layer. Future experiments will characterize the plasma properties during this radiative collapse, using time-resolved measurements of the layer width, temperature, density, and outflow velocity. The findings in this Letter are of particular relevance to the generation of radiative emission from reconnection-driven astrophysical events, and to the global dynamics of reconnection in strongly-cooled systems. These experiments also provide a novel platform for the investigation of radiative effects in HED and laboratory astrophysics experiments, and for validation of radiation (magneto-)hydrodynamic and atomic codes.

The authors would like to thank the Z machine operations teams and the target fabrication team for their contributions to this work. Experimental time on the Z facility was provided through the Z Fundamental Science Program. This work was funded by NSF and NNSA under grant no. PHY2108050, and by the NSF EAGER grant no. PHY2213898. RD acknowledges support from the MIT MathWorks and the MIT College of Engineering Exponent fellowships. DAU gratefully acknowledges support from NASA grants 80NSSC20K0545 and 80NSSC22K0828. This work was supported by Sandia National Laboratories, a multimission laboratory managed and operated by National Technology and Engineering Solutions of Sandia, LLC, a wholly owned subsidiary of Honeywell International Inc., for the U.S. Department of Energy's National Nuclear Security Administration under contract DE-NA0003525. This paper describes objective technical results and analysis. Any subjective views or opinions that might be expressed in the paper do not necessarily represent the views of the U.S. Department of Energy or the United States Government.

* Current address: Commonwealth Fusion Systems, Devens, MA 01434, USA

† jdhare@mit.edu

[1] E. N. Parker, J. Geophys. Res. **62**, 509 (1957).
[2] M. Yamada, R. Kulsrud, and H. Ji, Rev. Mod. Phys. **82**, 603 (2010).
[3] H. Ji, W. Daughton, J. Jara-Almonte, A. Le, A. Stanier, and J. Yoo, Nature Reviews Physics **4**, 263 (2022).
[4] J. Goodman and D. Uzdensky, ApJ **688**, 555 (2008).
[5] A. M. Beloborodov, ApJ **850**, 141 (2017).
[6] G. R. Werner, A. A. Philippov, and D. A. Uzdensky, Monthly Notices of the Royal Astronomical Society: Letters **482**, L60 (2019).
[7] J. Mehlhaff, G. Werner, D. Uzdensky, and M. Begelman, MNRAS **508**, 4532 (2021).
[8] Y. Lyubarsky and J. Kirk, ApJ **547**, 437 (2001).
[9] D. A. Uzdensky and A. Spitkovsky, ApJ **780**, 3 (2014).
[10] B. Cerutti, A. Philippov, K. Parfrey, and A. Spitkovsky, MNRAS **448**, 606 (2015).
[11] K. M. Schoeffler, T. Grismayer, D. Uzdensky, R. Fonseca, and L. Silva, Astrophys. J. **870**, 49 (2019).
[12] H. C. Spruit, F. Daigne, and G. Drenkhahn, Astron. Astrophys. **369**, 694 (2001).
[13] D. A. Uzdensky and A. I. MacFadyen, Phys. Plasmas **14** (2007), 10.1063/1.2721969.
[14] D. Giannios, Astron.Astrophys. **480**, 305 (2008).
[15] D. A. Uzdensky, Space Sci. Rev. **160**, 45 (2011).
[16] J. C. McKinney and D. A. Uzdensky, Monthly Notices of the Royal Astronomical Society **419**, 573 (2012).
[17] D. A. Uzdensky and J. C. McKinney, Phys. Plasmas **18**, 042105 (2011).
[18] D. A. Uzdensky, *Radiative magnetic reconnection in astrophysics* (Springer, 2016) p. 473.
[19] V. L. Dorman and R. M. Kulsrud, ApJ. **449**, 777 (1995).
[20] M. Yamada, H. Ji, S. Hsu, T. Carter, R. Kulsrud, N. Bretz, F. Jobes, Y. Ono, and F. Perkins, Phys. Plasmas **4**, 1936 (1997).
[21] H. Ji, M. Yamada, S. Hsu, R. Kulsrud, T. Carter, and S. Zaharia, Phys. Plasmas **6**, 1743 (1999).
[22] S. C. Hsu, G. Fiksel, T. Carter, H. Ji, R. Kulsrud, and M. Yamada, Phys. Rev. Lett. **84**, 3859 (2000).
[23] Y. Ren, M. Yamada, S. Gerhardt, H. Ji, R. Kulsrud, and A. Kuritsyn, Phys. Rev. Lett. **95**, 055003 (2005).
[24] M. Rosenberg, C. Li, W. Fox, A. Zylstra, C. Stoeckl, F. Séguin, J. Frenje, and R. Petrasso, Phys. Rev. Lett. **114**, 205004 (2015).
[25] P. Nilson, L. Willingale, M. Kaluza, C. Kamperidis, S. Minardi, M. Wei, P. Fernandes, M. Notley, S. Bandyopadhyay, M. Sherlock, *et al.*, Phys. Rev. Lett. **97**, 255001 (2006).
[26] C. Li, F. Séguin, J. Frenje, J. Rygg, R. Petrasso, R. Town, O. Landen, J. Knauer, and V. Smalyuk, Phys. Rev. Lett. **99**, 055001 (2007).
[27] G. Fiksel, W. Fox, A. Bhattacharjee, D. Barnak, P.-Y. Chang, K. Germaschewski, S. Hu, and P. Nilson, Phys. rev. Lett. **113**, 105003 (2014).
[28] A. Chien, L. Gao, S. Zhang, H. Ji, E. G. Blackman, W. Daughton, A. Stanier, A. Le, F. Guo, R. Follett, *et al.*, Nature Physics **19**, 254 (2023).
[29] W. Fox, A. Bhattacharjee, and K. Germaschewski, Phys. Plasmas **19**, 056309 (2012).
[30] S. Lebedev, A. Frank, and D. Ryutov, Rev. Mod. Phys. **91**, 025002 (2019).
[31] L. Suttle, J. Hare, S. Lebedev, G. Swadling, G. Burdiak, A. Ciardi, J. Chittenden, N. Loureiro, N. Niasse, F. Suzuki-Vidal, *et al.*, Phys. rev. Lett. **116**, 225001 (2016).
[32] J. Hare, L. Suttle, S. Lebedev, N. Loureiro, A. Ciardi, J. Chittenden, T. Clayson, S. Eardley, C. Garcia, J. Halliday, *et al.*, Phys. Plasmas **25**, 055703 (2018).

[33] J. Hare, L. Suttle, S. Lebedev, N. Loureiro, A. Ciardi, G. Burdiak, J. Chittenden, T. Clayson, C. Garcia, N. Niasse, *et al.*, Phys. Rev. Lett. **118**, 085001 (2017).

[34] L. Suttle, J. Hare, S. Lebedev, A. Ciardi, N. Loureiro, G. Burdiak, J. Chittenden, T. Clayson, J. Halliday, N. Niasse, *et al.*, Phys. Plasmas **25**, 042108 (2018).

[35] D. Sinars, M. Sweeney, C. Alexander, D. Ampleford, T. Ao, J. Apruzese, C. Aragon, D. Armstrong, K. Austin, T. Awe, *et al.*, Phys. Plasmas **27**, 070501 (2020).

[36] R. Datta, A. J. Crilly, J. P. Chittenden, S. Chowdhry, K. Chandler, N. Chaturvedi, C. E. Myers, W. R. Fox, S. B. Hansen, C. A. Jennings, H. Ji, C. C. Kuranz, S. V. Lebedev, D. A. Uzdensky, and J. D. Hare, arXiv (2024), 10.48550/arXiv.2401.01795, 2401.01795.

[37] D. Uzdensky, N. Loureiro, and A. Schekochihin, Phys. Rev. Lett. **105**, 235002 (2010).

[38] A. Ciardi, S. Lebedev, A. Frank, E. Blackman, J. Chittenden, C. Jennings, D. Ampleford, S. Bland, S. Bott, J. Rapley, *et al.*, Phys. Plasmas **14**, 056501 (2007).

[39] A. Crilly, N. Niasse, A. Fraser, D. Chapman, K. McLean, S. Rose, and J. Chittenden, High Energy Density Physics , 101053 (2023).

[40] J. Hare, S. Lebedev, L. Suttle, N. Loureiro, A. Ciardi, G. Burdiak, J. Chittenden, T. Clayson, S. Eardley, C. Garcia, *et al.*, Phys. Plasmas **24**, 102703 (2017).

[41] T. Webb, D. Bliss, G. Chandler, D. Dolan, G. Dunham, A. Edens, E. Harding, M. Johnston, M. Jones, S. Langendorf, *et al.*, Rev. Sci. instrum. **94** (2023), 10.1063/5.0123448.

[42] A. Porwitzky and J. Brown, Phys. Plasmas **25** (2018), 10.1063/1.5026983.

[43] A. Harvey-Thompson, S. Lebedev, S. Bland, J. Chittenden, G. Hall, A. Marocchino, F. Suzuki-Vidal, S. Bott, J. Palmer, and C. Ning, Physics of Plasmas **16** (2009), 10.1063/1.3077305.

[44] R. Datta, J. Angel, J. B. Greenly, S. N. Bland, J. P. Chittenden, E. S. Lavine, W. M. Potter, D. Robinson, T. W. O. Varnish, E. Wong, D. A. Hammer, B. R. Kusse, and J. D. Hare, Physics of Plasmas **30**, 092104 (2023).

[45] M. Cuneo, E. Waisman, S. Lebedev, J. Chittenden, W. Stygar, G. Chandler, R. Vesey, E. Yu, T. Nash, D. Bliss, *et al.*, Physical Review E **71**, 046406 (2005).

[46] T. Byvank, J. Banasek, W. Potter, J. Greenly, C. Seyler, and B. Kusse, Phys. Plasmas **24** (2017), 10.1063/1.3079752.

[47] R. Datta, D. Russell, I. Tang, T. Clayson, L. Suttle, J. Chittenden, S. Lebedev, and J. Hare, Rev. Sci. Instrum. **93**, 103530 (2022).

[48] R. Datta, D. R. Russell, I. Tang, T. Clayson, L. G. Suttle, J. P. Chittenden, S. V. Lebedev, and J. D. Hare, J. Plasma Phys. **88**, 905880604 (2022).

[49] M. Schaeuble, T. Nagayama, J. Bailey, B. Dunlap, and S. Patel, Phys. Plasmas **28** (2021), 10.1063/5.0047931.

[50] J. MacFarlane, I. Golovkin, P. Wang, P. Woodruff, and N. Pereyra, High energy density physics **3**, 181 (2007).

[51] R. Datta, F. Ahmed, and J. D. Hare, IEEE Transactions on Plasma Science , 1 (2024).

[52] L. Claus, L. Fang, R. Kay, M. Kimmel, J. Long, G. Robertson, M. Sanchez, J. Stahoviak, D. Trotter, and J. Porter, Target Diagnostics Physics and Engineering for Inertial Confinement Fusion IV **9591**, 177 (2015).

[53] E. Harding, T. Ao, J. Bailey, G. Loisel, D. Sinars, M. Geissel, G. Rochau, and I. Smith, Rev. Sci. Instrum. **86** (2015), 10.1063/1.4918619.

[54] S. Hansen, J. Bauche, C. Bauche-Arnoult, and M. Gu, High Energy Density Physics **3**, 109 (2007).

[55] R. Drake, *High-Energy-Density Physics. Fundamentals, Inertial Fusion and Experimental Analysis* (Springer, 2013).

[56] N. Loureiro, A. Schekochihin, and S. Cowley, Phys. Plasmas **14**, 100703 (2007).

[57] A. Richardson, *NRL plasma formulary* (US Naval Research Laboratory, 2019).

[58] R. Ying and G. Kalman, Physical Review A **40**, 3927 (1989).

[59] W. Fox, A. Bhattacharjee, and K. Germaschewski, Phys. Rev. Lett. **106**, 215003 (2011).

[60] J. Olson, J. Egedal, M. Clark, D. A. Endrizzi, S. Greess, A. Millet-Ayala, R. Myers, E. E. Peterson, J. Wallace, and C. B. Forest, J. Plasma Phys. **87**, 175870301 (2021).

[61] J. P. Goedbloed, R. Keppens, and S. Poedts, *Advanced Magnetohydrodynamics: With Applications to Laboratory and Astrophysical Plasmas* (Cambridge University Press, 2010).

[62] T. J. M. Boyd and J. J. Sanderson, *The Physics of Plasmas* (Cambridge University Press, 2003).

[63] R. Samtaney, N. Loureiro, D. Uzdensky, A. Schekochihin, and S. Cowley, Physical review letters **103**, 105004 (2009).